


Review

Characteristics of Critical-Wavelength-Existed Fiber-Optic Mach–Zehnder Interferometers and Their Sensing Applications

Chenxu Lu ¹, Xiaopeng Dong ^{2,*} and Chi Wu ¹

¹ Southern Marine Science and Engineering Guangdong Laboratory (Guangzhou), Guangzhou 511458, China; chenxulu@gmlab.ac.cn (C.L.); qi.wu@gmlab.ac.cn (C.W.)

² Department of Electronic Engineering, School of Electronic Science and Engineering, Xiamen University, Xiamen 361005, China

* Correspondence: xpd@xmu.edu.cn

Abstract: In this paper, we review the characteristics of critical wavelength (CWL)-existed fiber-optic Mach–Zehnder interferometers (MZIs), including special few-mode fibers and microfibers, and their sensing applications in physical, chemical, and marine fields. Owing to the existence of CWL in the transmission spectra, the in-line MZIs show some specific characteristics. The closer the peak/dip wavelength to the CWL, the larger the wavelength shift or the related sensitivity when the interferometer is under testing. Meanwhile, CWL shifts monotonically with the variations in measurands, such as temperature (in the air or seawater), axial strain, water pressure, surrounding refractive index, etc., when they are applied to the sensing fibers. These characteristics of the CWL-existed in-line MZIs make them appealing solutions for fabricating various interferometric sensors, with the advantages of large measurement range, high sensitivity, multiparameter sensing, etc. Theoretical and experimental studies on the properties of the CWL-existed in-line MZIs are reviewed and discussed in this paper.

Keywords: fiber-optic sensors; few-mode fiber; microfiber; Mach–Zehnder interferometer; critical wavelength



Citation: Lu, C.; Dong, X.; Wu, C. Characteristics of Critical-Wavelength-Existed Fiber-Optic Mach–Zehnder Interferometers and Their Sensing Applications. *Photonics* **2022**, *9*, 378. <https://doi.org/10.3390/photonics9060378>

Received: 7 April 2022

Accepted: 12 May 2022

Published: 26 May 2022

Publisher's Note: MDPI stays neutral with regard to jurisdictional claims in published maps and institutional affiliations.



Copyright: © 2022 by the authors. Licensee MDPI, Basel, Switzerland. This article is an open access article distributed under the terms and conditions of the Creative Commons Attribution (CC BY) license (<https://creativecommons.org/licenses/by/4.0/>).

1. Introduction

Fiber-optic in-line Mach–Zehnder interferometers (MZIs) have the advantages of high sensitivity, compact size, flexible structure, immunity to electromagnetic interference, and durability in harsh and corrosive environments and, therefore, have been intensively studied and applied in physical, chemical, and marine sensing fields, to monitor a considerable variety of essential parameters [1–5]. An in-line MZI can be constructed by splicing a piece of few-mode fiber (FMF) between two pieces of single-mode fibers (SMF)—termed SFS structure [6–15]—or replacing the FMF with the multimode fiber (MMF) [16–21], two-core fiber [22], thin-core fiber [23], no-core fiber [24], photonic crystal fiber [25] and few-mode microfiber [26–36], where offset fusion splicing [37], fiber taper [38], and collapsed splicing [39] are often used in the fabrication.

A typical in-line MZI shows periodic interference fringes. The interference peaks/dips in the periodically changed transmission spectrum exhibit the same behavior, i.e., shifting in the same direction, with the same sensitivity, when monitoring sensing parameters. In this case, when such a sensor system is being applied to detect any particular parameter through monitoring the wavelength variations of a specific interference peak/dip or intensity variations at a particular wavelength, some critical issues will limit the veracity of the sensor performance: (1) multivalued outputs and limited measurement range induced by overlapping of adjacent peaks/dips; (2) limitations in multiparameter applications caused by the uniformity of the interference fringes and their wavelength sensitivity.

However, in the transmission spectra of some in-line MZIs, a critical wavelength (CWL) may appear in the operating wavelength range. At the CWL, the wavelength

response period seen is infinite in the transmission spectrum. This interference fringe, which shows the least dependence on wavelength, is defined as the achromatic fringe [26]. In fact, the CWL is the wavelength at which the two interference modes' group velocities equal each other. Therefore, the propagation constant difference in the two interference modes changes nonlinearly with wavelength and turns around at CWL. In this way, the CWL is also called the dispersion turning point (DTP).

The CWL-existed in-line MZIs exhibit intriguing characteristics that researchers have thoroughly studied and applied in a wide range of sensing fields: (1) The peak lying closest to CWL at each side has its maximum spacing from the adjacent peak. Thus, compared with periodically changed interference fringes, the CWL is easy to identify in the transmission spectrum. Moreover, the CWL is exclusive at the operating wavelength range, which becomes an excellent candidate for measuring various parameters, especially in large-range measurement. (2) The interference peak/dip closest to the CWL has the maximum wavelength sensitivity among all the interference peaks/dips. (3) The interference peaks/dips on each side of the CWL shift to opposite directions under sensing parameter variations. The characteristics of the CWL and the interference peaks/dips have been proved with competitive advantages in large-range measurement [7,8,30], high wavelength sensitivities of interference peaks/dips [10,28–33,35,36], and co-located multiparameter sensing [9,11]. With these advantages, the CWL-existed in-line MZIs have been reported in sensing parameters of axial strain, curvature, displacement, surrounding refractive index, temperature, relative humidity, static pressure, chemical solution concentration, etc., according to the particular circumstances. Difference fibers such as liquid-core fiber, MMF, FMF, and few-mode microfibers are employed in these CWL-existed in-line MZIs.

In this paper, we provide a simple but overall review of the developments and recent progress on CWL-existed in-line MZIs and their sensing applications. In Section 2, the generation of the CWL is explained. In Section 3, we review the wavelength sensitivity characteristics of the interference peaks/dips lying near the CWL and their applications in sensors. The large-range measurement sensors employing CWL detection are reviewed in Section 4. Lastly, in Section 5, some conclusions and prospects are given.

2. Theoretical Analysis of the Transmission Characteristics of the CWL-Existed in-Line MZIs

CWL has been experimentally observed in different kinds of in-line MZIs employing MMFs [17–20], FMFs [6–15], liquid-core fibers [40], tapered few-mode microfibers [25–35], highly birefringent (HB) fibers [41] or birefringent side-hole fibers [42]. The mode interferences in these CWL-existed in-line MZIs are mainly between the fundamental mode and the first circularly symmetric high-order mode or the first antisymmetric high-order mode and between two orthogonal (x and y) polarization modes. The schematic diagram of the sensor system is shown in Figure 1. Compared with mode interference, where the polarization-dependent light is included, the in-line MZI with two circularly symmetric modes interference provides merits of stability and polarization independence [43]. As an example, in this section, we use an SFS structure reported by our group in references [6–14], in which the LP₀₁ and LP₀₂ mode interferences were employed, to explain the transmission characteristics of the CWL-existed MZIs theoretically.

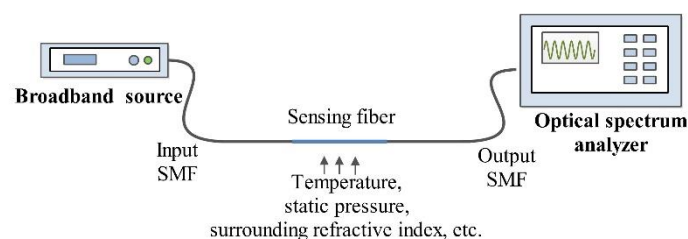


Figure 1. Schematic of the critical-wavelength-existed in-line Mach-Zehnder interferometer measurement system.

Figure 2 shows the cross-section structure of the FMF and the schematic diagram of the SFS structure. The relative refractive index difference is defined as $\Delta n_{co/cli} = (n_{co/cli} - n_0) / n_0$, where the $n_{co/cli}$ and n_0 are the refractive indices of the core/ i^{th} inner cladding and pure silica of the FMF, respectively. FMF is specially designed with five layers and a W-shaped refractive index difference profile. Therefore, at the operational wavelength planned, the FMF supports only the LP₀₁ and LP₀₂ modes propagating in the fiber under well-centered splicing [44].

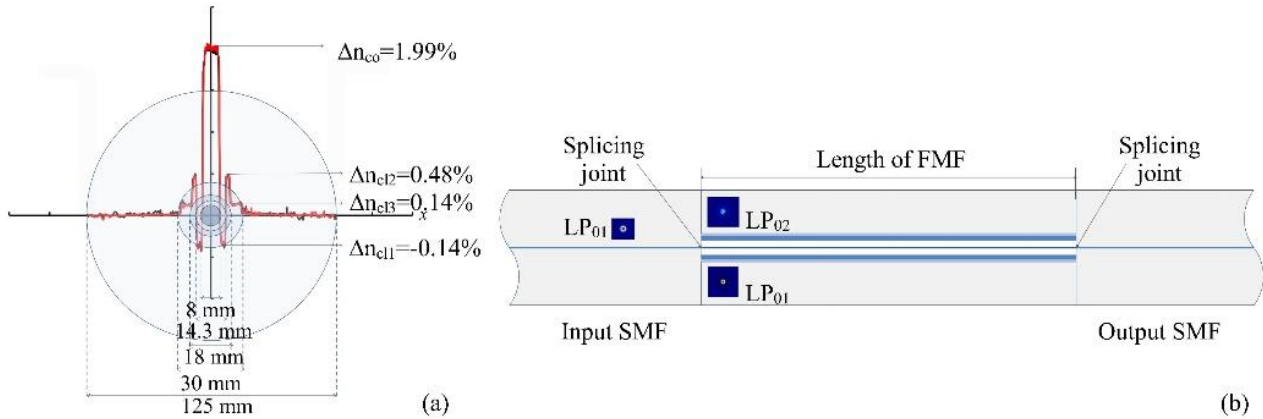


Figure 2. (a) Geometrical structure and relative refractive index difference profile of the few-mode fiber; (b) the SMF–FMF–SMF (SFS) structure. The insets are simulated mode field distributions of the LP₀₁ mode propagating in SMF and the LP₀₁ and LP₀₂ modes propagating in FMF at 1550 nm wavelength using the finite element model. SMF: single-mode fiber; FMF: few-mode fiber.

The LP₀₁ and LP₀₂ modes propagating in the FMF are excited by the fundamental mode LP₀₁ in input SMF. The interference between the LP₀₁ and LP₀₂ modes is transmitted by output SMF. The ratios of optical power transferred to the LP₀₁ and LP₀₂ modes in the FMF from input SMF are $t_{01} = P_{01} / P_{in}$ and $t_{02} = P_{02} / P_{in}$, and calculated as 81% and 11.5%, respectively. The transmission, T, through the SFS structure with L_{FMF} -length FMF is given by [15] as follows:

$$T = \frac{P_{out}}{P_{in}} = t_{01}^2 + t_{02}^2 + 2t_{01}t_{02}\cos(\varphi(\lambda)) \tag{1}$$

where $\varphi(\lambda) = \Delta\beta \cdot L_{FMF}$ is the phase difference between LP₀₁ and LP₀₂ modes. $\Delta\beta$ is the propagation constant difference between LP₀₁ and LP₀₂ modes.

With the parameters of FMF given in Figure 1, a finite element model is established to simulate the relationship between the $\Delta\beta$ and wavelength, which is depicted as a dashed line in Figure 3. The calculated transmission spectrum combining Equation (1) and the simulated value of $\Delta\beta$ is shown as a solid line in Figure 3, where the physical length of the employed FMF is 50 cm. Because the dispersion of $\Delta\beta$ exhibits nonlinear behavior and has a maximum, corresponding to the value of CWL in the transmission spectrum at the operational wavelength, the wavelength response period at CWL is infinite. Moreover, the periods of interference fringes closest to CWL from both sides reach a maximum. As shown in Figure 3, numbering from the peak that lies closest to CWL from each side, the peaks that are located on the higher wavelength side of CWL (i.e., within the region from CWL to 1580 nm) are denoted as $P_{H,1}, P_{H,2}, \dots$, respectively. Peaks located on the lower wavelength side of CWL (i.e., within the region from 1530 nm to CWL) are denoted as $P_{L,1}, P_{L,2}, \dots$, respectively. The interference dips are also numbered in the same way.

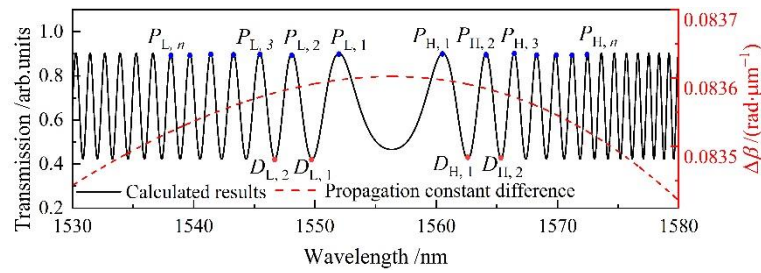


Figure 3. The simulated curve of the propagation constant difference $\Delta\beta$ of LP₀₁ and LP₀₂ modes propagating in the few-mode fiber, and the transmission spectrum of the SFS structure ($L_{\text{FMF}} = 50$ cm) under the temperature of 25 °C versus wavelength.

With the achromatic fringes in the transmission spectrum, multiple sensing indicators are provided in the sensors employing CWL-existed in-line MZIs, including monitoring wavelength shifts in CWL [6–8,18,40], $P_{H,1}/D_{H,1}$, $P_{L,1}/D_{L,1}$ [9–11,15,17,28–36], and intensity variations [12] at a specific wavelength or wavelength ranges. Studies in CWL-existed in-line MZIs show that utilizing CWL shifts or other monitoring parameters listed above, the CWL-existed in-line MZIs can provide competitive advantages over conventional periodically changed interferometers in the applications of large-range measurement, co-located multiparameter sensing, and high-sensitivity sensing. Moreover, the theoretical study of wavelength sensitivities of interference fringes offers a direction for mode interferometers to maximize their peak wavelength sensitivities.

3. Characteristics of Interference Peaks/Dips in the CWL-Existed in-Line MZIs and Their Applications

In a CWL-existed transmission spectrum, the interference peaks/dips, especially those lying closest to CWL on both sides, exhibit essential characteristics different from the typical periodically changing fringes. These differences were experimentally observed by Salik et al. [15] and Zhou et al. [17]. However, theoretical analysis was not presented. The wavelength sensitivities of the interference fringes under temperature, axial strain, static pressure, and surrounding refractive index (SRI) variations were further theoretically and experimentally studied in Refs. [10,11,28–30,32,36], which are reviewed in this section.

3.1. Characteristics of Interference Peaks/Dips in the CWL-Existed SFS Structures

For the CWL-existed SFS structure employing the FMF shown in Figure 2, because the geometrical structure and relative refractive index difference profile of the FMF are determined, the temperature, axial strain, and static pressure wavelength sensitivities of the interference peaks/dips are governed by the wavelength separations between the measured wavelengths and the CWL. The temperature (T), axial strain (ϵ), and static pressure (P) wavelength sensitivities can be written as follows [11,13]:

$$\frac{\Delta\lambda}{\Delta T} = -\left(\frac{\partial(\Delta\beta)}{\partial T} + \Delta\beta \cdot \alpha\right) \left(\frac{\partial(\Delta\beta)}{\partial\lambda}\right)^{-1} \tag{2}$$

$$\frac{\Delta\lambda}{\Delta\epsilon} = -\left(\Delta\beta + \frac{k_0^2}{2\beta_1\beta_2} \left(\gamma(n_0^4\Delta\beta + (n_{co}^4 - n_0^4)(\beta_1b_1 - \beta_2b_2)) + V\delta\left(\beta_1\frac{\partial b_1}{\partial V} - \beta_2\frac{\partial b_2}{\partial V}\right)\right)\right) \left(\frac{\partial(\Delta\beta)}{\partial\lambda}\right)^{-1} \tag{3}$$

$$\frac{\Delta\lambda}{\Delta P} = -\left(\frac{-(1-2\nu)}{E}\Delta\beta + \frac{k_0(1-2\nu)}{2E}(2\rho_{12} + \rho_{11})(n_1^3 - n_2^3) - \frac{(1-2\nu)V^3}{2r_{co}^2E} \left(\frac{1}{\beta_1}\frac{\partial b_1}{\partial V} - \frac{1}{\beta_2}\frac{\partial b_2}{\partial V}\right)\right) \left(\frac{\partial(\Delta\beta)}{\partial\lambda}\right)^{-1} \tag{4}$$

where β_{01} and β_{02} are the propagation constants of the LP₀₁ and LP₀₂ modes, respectively. $\alpha = (1/L_{FMF})(\partial L_{FMF}/\partial T) = 5.1 \times 10^{-7}/^\circ\text{C}$ is the thermal expansion coefficient for pure silica [20]. $\gamma = \rho_{12} - \nu(\rho_{11} + \rho_{12})$ and $\delta = \nu(n_{co}^2 - n_0^2) + (\gamma/2)(n_{co}^4 - n_0^4)$. $\rho_{11} = 0.12$, $\rho_{12} = 0.27$ are strain-optic coefficients for fused silica, respectively [45]. $\nu = 0.17$ and $E = 78$ GPa is the Poisson ratio and Young’s modulus for pure silica, respectively [46]. $k_0 = 2\pi/\lambda$ is the free space wave vector. r_{co} is the core radius of the FMF. n_1 and n_2 is the effective refractive index of the LP₀₁ and LP₀₂ modes propagating in the FMF, respectively. $V = k_0 r_{co} \sqrt{n_{co}^2 - n_0^2}$ is the normalized frequency of the FMF. β_i and b_i ($i = 1, 2$) is the propagation constant and normalized propagation constant of LP_{0i} mode, respectively, and can be represented as

$$\beta_i^2 = k_0^2 \left(n_0^2 + b_i (n_{co}^2 - n_0^2) \right) \tag{5}$$

The wavelength sensitivity curves under temperature, axial strain, and static pressure are calculated and depicted in solid curves in Figure 4a–c, together with the experimental results. From Equations (2)–(5) and Figure 4, the wavelength sensitivities of interference fringes in the spectrum of the SFS structure with CWL can be summarized as follows:

- (1) The interference peaks/dips lying on the different sides of the CWL shift to opposite directions under temperature, axial strain, and static pressure variations. For example, when temperature increases, there is a blueshift for peaks on the lower wavelength side of the CWL (i.e., within the region from 1500 nm to the CWL), while for peaks on the longer wavelength side of the CWL (i.e., within the region from the CWL to 1580 nm), there is a redshift. The experimental transmission spectra of the SFS structure under temperature variations are shown in Figure 4d, which agrees well with the calculation results.
- (2) The wavelength sensitivity of the interference peak is only related to the wavelength spacing between the measured wavelength and the CWL. The L_{FMF} used in the SFS sensor and the sensing parameters pre-applied to the FMF section may change the wavelength separation between the peak wavelength and the CWL. Thus, the variation in wavelength separation will affect the corresponding wavelength sensitivity of the measured peaks, as shown in Figure 4a–c. The experimental results show close agreement with the simulated curves.
- (3) As the peak wavelength value approaches the CWL value, i.e., $\lambda/\lambda_{CWL} \rightarrow 1$, the wavelength sensitivity increases significantly, as shown in Figure 4a–c, from both the theoretical and experimental points of view. However, the mathematically derived infinitely high sensitivity at the CWL has no practical meaning because $\partial(\Delta\beta)/\partial\lambda = 0$ at CWL from the theoretical analysis, and an infinite length of FMF is needed in experiments to minimize the wavelength spacing between the wavelength of P_{L,1}/P_{H,1}, and the CWL, which is unpractical in applications.

Because the wavelength sensitivities of interference peaks and CWL are different under sensing parameter variations, the SFS structure can be applied in multiparameter sensing by simultaneously measuring the shift in CWL and interference peaks. Simultaneous measurements of temperature and axial strain [9] have been studied by detecting wavelength shifts in P_{H,1} and P_{L,1}, taking advantage of their highest wavelength sensitivities among all of the peaks on the right and left sides of the CWL, respectively.

To further improve the sensitivity performance, a cascaded CWL-existed SFS structure was proposed by our group, which has been applied in static water pressure and temperature sensing [11]. Figure 5 shows the schematic diagram and transmission spectra under different static water pressures of the cascaded SFS structure. Vernier effect was adopted to magnify the wavelength sensitivities of interference peaks. The free spectrum range of the envelope in the superimposed transmission spectra varies with wavelength and reaches the maximum when approaching the envelope critical wavelength (CWL_E). Therefore, the envelop peaks, P_{EL,1} and P_{EL,2}, are easy to identify. A maximum static water pressure sensitivity of 4.072 nm/MPa and temperature sensitivity of 1.753 nm/°C

is achieved using this sensing approach, which is more than 7 times larger in terms of the wavelength sensitivity than those reported in sensors using a single CWL-existed SFS structure [14]. This cascaded CWL-existed SFS static-pressure sensor can be applied in marine pressure sensing with temperature compensation by simultaneously measuring the envelope peaks $P_{EL,1}$ and $P_{EL,2}$.

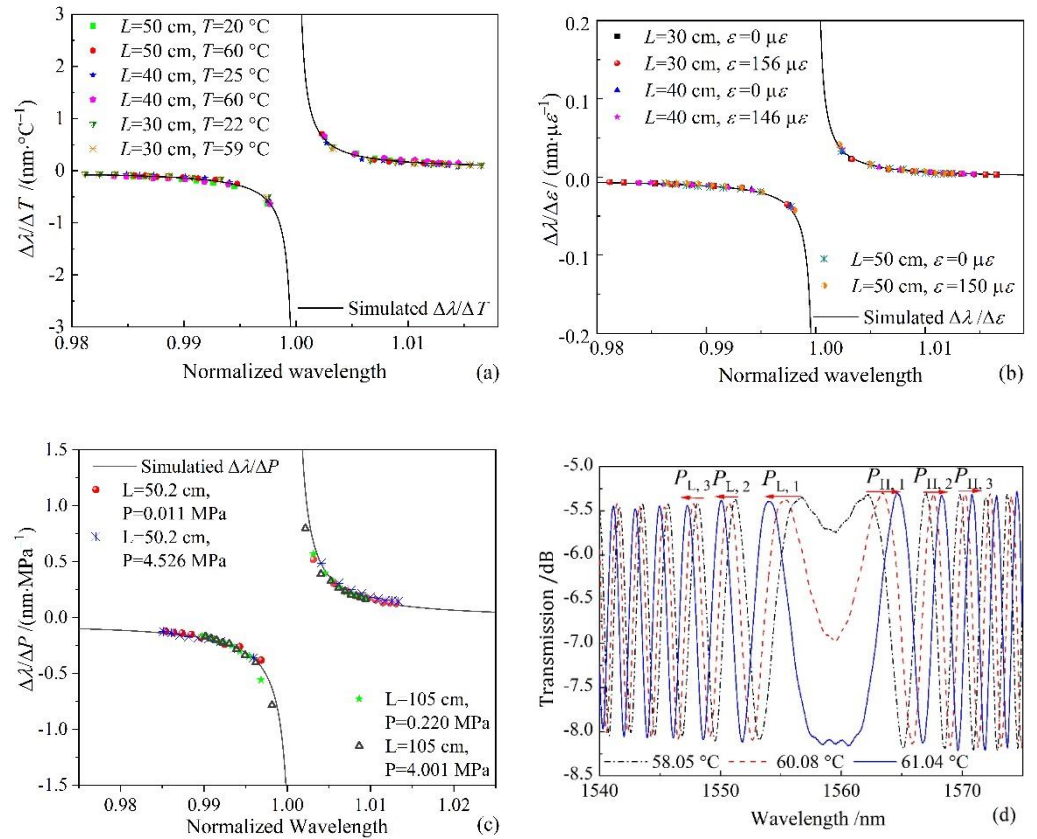


Figure 4. Characteristics of interference fringes in the transmission spectra of the CWL-existed SFS structure: (a) temperature wavelength sensitivities of interference fringes; (b) axial strain wavelength sensitivities of interference fringes; (c) static pressure wavelength sensitivities of interference fringes; (d) transmission spectra of the SFS structure ($L_{FMF} = 50$ cm) under temperature variations.

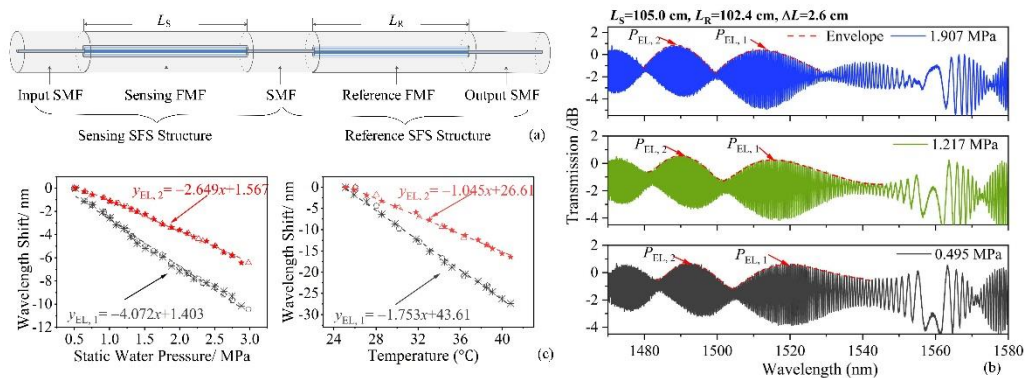


Figure 5. (a) Diagram of the cascaded SMF-FMF-SMF(SFS) structure; (b) experimental transmission spectra of the cascaded SFS structure under static water pressure variations; (c) wavelength shifts in $P_{EL,1}$ and $P_{EL,2}$ under static water pressure and temperature variations. Reprinted with permission from ref. [11]. Copyright 2020 IEEE.

3.2. Characteristics of Interference Peaks/Dips in the CWL-Existed Few-Mode Microfiber in-Line MZIs

The few-mode microfiber interferometer fabricated by tapering a normal-sized optical fiber to the diameter of several micrometers is widely applied in SRI sensing using the evanescent waves propagating in the microfiber section. Wei et al. [28] proposed a few-mode microfiber interferometer designed at the CWL. They explored the SRI sensing properties of tapered microfiber interferometers in a gaseous medium, where the SRI changes around 1. The nonadiabatic few-mode microfiber is tapered from a standard SMF. The fundamental HE₁₁ mode and the high-order HE₁₂ mode are excited and propagate in the uniform waist region, as shown in Figure 6.

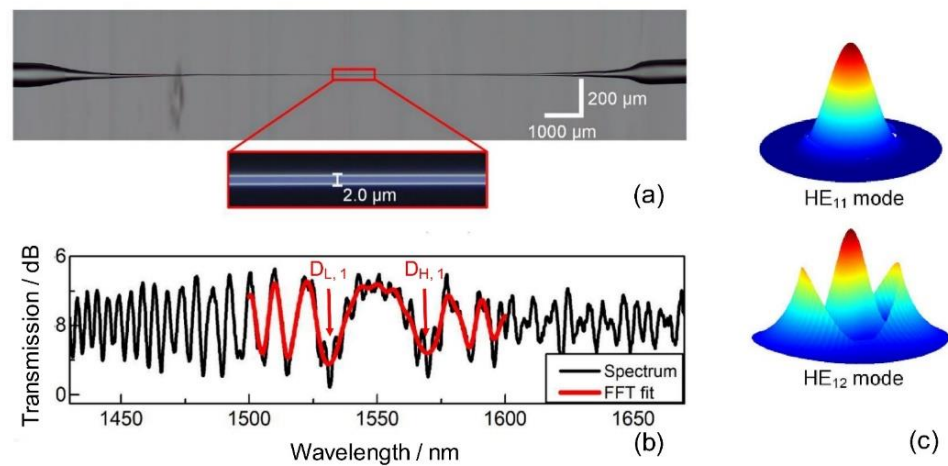


Figure 6. (a) The microscopic view of the tapered optical microfiber; (b) the origin (black) and the fast Fourier transform (FFT)-filtered (red) transmission spectra of the tapered few-mode microfiber surrounded by air; (c) the simulated mode profiles of HE₁₁ and HE₁₂ modes. Adapted with permission from [28].

For a particular interference peak/dip with the peak/dip wavelength of λ_N , the SRI wavelength sensitivity is written as follows [28,47]:

$$\frac{\Delta\lambda_N}{\Delta SRI} = \frac{\lambda_N}{G} \frac{\partial(\Delta n_{eff})}{\partial n} \tag{6}$$

where $G = n_g^{HE_{11}} - n_g^{HE_{12}}$ is the difference between the group effective index of HE₁₁ and HE₁₂ modes. The group effective index can be calculated by $n_g = n_{eff} - \lambda_N \partial(n_{eff}) / \partial \lambda_N$. Therefore, with known material and diameter parameters of the uniform microfiber section, the term $\Delta\lambda_N / \Delta SRI$ increases dramatically as the value of G approaches zero, which corresponds to the CWL point. Moreover, the interference peaks/dips lying on each side of the CWL shift to opposite wavelength directions under SRI variations. These conclusions agree well with the wavelength sensitivity study of CWL-existed SFS structure. The calculated wavelength sensitivity curves of SRI under different microfiber diameters are shown in Figure 7. By measuring the peak wavelength separation of D_{L,1} and D_{H,1}, a maximum sensitivity of $-69,984.3$ nm/RIU (“-” denotes blue wavelength shifts) around the air refractive index is obtained in experiments. The temperature influence on the gas RI sensor is also reported, and the measured temperature sensitivities of D_{L,1} and D_{H,1} are -2.134 nm/°C and 1.899 nm/°C, respectively. Thus, the cross-sensitivity of the gas refractive index sensor is 5.763×10^{-5} RIU/°C.

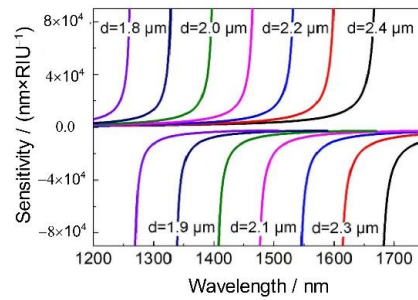


Figure 7. The surrounding refractive index sensitivities of interference fringes around CWLs at different waist diameters of microfibers. Adapted with permission from Ref. [28].

With the merits of excellent sensitivity performances and simple fabrication processes, few-mode microfibers have been further studied and applied in various SRI-related sensing parameters. Guan et al. [29] thoroughly investigated the sensitivity of a two-mode microfiber MZI as a function of SRI. Since Equation (7) can be rewritten as

$$\frac{\Delta\lambda_N}{\Delta n_{SRI}} = \lambda_N \frac{1}{\Gamma} \left(\frac{1}{\Delta n_{eff}} \frac{\partial(\Delta n_{eff})}{\partial n_{SRI}} \right) \tag{7}$$

where $\Gamma = 1 - \lambda_N / \Delta n_{eff} \cdot \Delta n_{eff} / \partial \lambda$ is a dispersion factor that characterizes the effect of index difference variations with wavelength, $\Delta n_{eff} / \partial \lambda$. Since the whole term in the bracket was negative [48], the sign of Γ is crucial in determining the SRI sensitivity sign. CWL exists at the point where the sign of the SRI sensitivity changes. The simulated dispersion factors Γ and $\Delta\lambda_N / \Delta n_{SRI}$ as functions of the fiber diameter is shown in Figure 8. The numerical simulation revealed that two CWLs exist as the microfiber diameter decreases. Experiments were conducted to study the wavelength sensitivities of interference fringes around both CWLs. At the second CWL, an ultrahigh SRI sensitivity of approximately 95,836 nm/RIU with the microfiber diameter of 1.87 μm was achieved around the SRI of air. Wang et al. [33] applied the few-mode microfiber MZI in marine fields by measuring sodium nitrate in seawater. They achieved the wavelength sensitivity of 5.98 pm/ppm using $D_{L,1}$, corresponding to the SRI sensitivity of 50,396.09 nm/RIU. CWL was also observed in Z-shaped few-mode microfibers between the interference of HE_{11} and HE_{21} modes [34]. The SRI sensitivity of 1.46×10^5 nm/RIU was experimentally achieved around the refractive index of water.

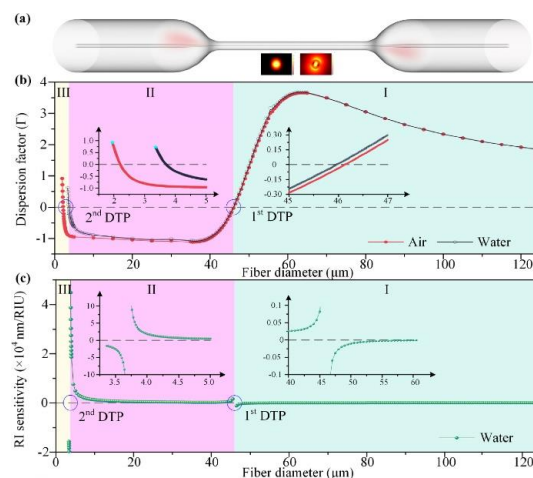


Figure 8. (a) Schematic diagram of the taper-based in-line MZI; the inset presents calculated intensity profiles of the interference two modes, HE_{11} and HE_{12} , respectively; (b) simulated dispersion factor Γ and (c) RI sensitivity as functions of the fiber diameter. Adapted with permission from Ref. [29].

Zhao et al. [32] demonstrated an ultrasensitive sensor for SRI and temperature measurement by employing a CWL-existed two-mode microfiber. An ultrahigh SRI sensitivity of 24,209 nm/RIU around 1.3320 and a high-temperature sensitivity of -2.47 nm/°C were experimentally achieved by a microfiber with a waist diameter of ~ 4.8 μm . Meanwhile, the CWL-existed microfiber was coated with a polydimethylsiloxane (PDMS) layer to increase the temperature sensitivity to about 8.33 nm/°C. To further increase the measurement range of the interference dips, they [30] proposed a fiber Bragg grating (FBG) cascaded microfiber in-line MZI operating at the CWL and applied it in seawater temperature measurement, as shown in Figure 9a. The FBG resonant dip, located in the achromatic fringe region, works as a rough measurement tool to identify the temperature measurement ranges. Meanwhile, the interference dip closest to the CWL with the highest sensitivity among all the interference dips was employed to measure the water temperature once the rough range was determined. The two-mode microfiber MZI was packaged in PDMS to increase temperature sensitivity. The transmission spectrum of the FBG-cascaded two-mode microfiber MZI in PDMS package is shown in Figure 9b. With the aid of FBG, the temperature measurement range could be enlarged from ~ 2 °C to ~ 36 °C, with a temperature sensitivity of ~ 38 nm/°C, as shown in Figure 9c.

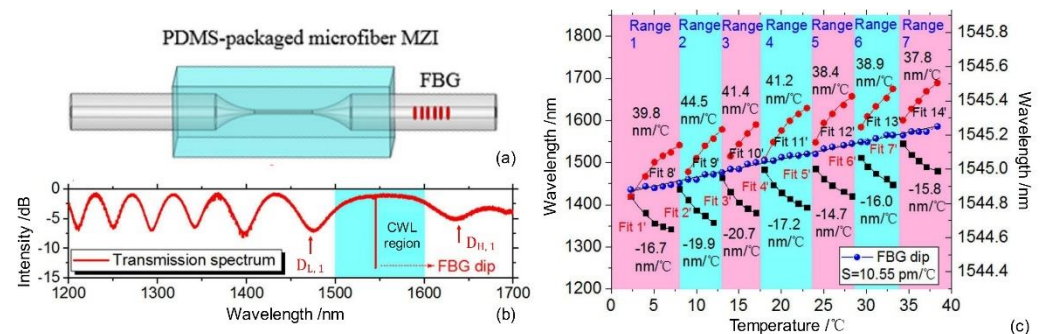


Figure 9. (a) Schematic of the polydimethylsiloxane (PDMS)-packaged two-mode microfiber for temperature measurement; (b) the transmission spectrum of the PDMS-packaged two-mode microfiber MZI cascaded with FBG; (c) cooperation of the FBG resonant dip and the interference dips ($D_{L,1}$ and $D_{H,1}$) lying on each side of the CWL in temperature measurement. Reprinted with permission from Ref. [30]. Copyright 2020 Elsevier.

Apart from using nonadiabatic tapers to fabricate the few-mode microfibers by tapering a standard SMF, other special fibers were employed to increase the sensor performance and redshift the cutoff wavelength of the high-order mode in the microfiber. In 2020, Wang et al. [31] proposed a CWL-existed in-line MZI by tapering a ring-core two-mode fiber. Quasi-adiabatic transition tapers were fabricated to provide HE_{11} and HE_{21} modes with continuous mode evolutions to the microfiber section. The two modes launched into the fiber were collected at the fiber output. A CWL was observed when the tapered two-mode microfiber was immersed in a liquid environment. The SRI sensitivities of 79,283.7 nm/RIU and $-48,772$ nm/RIU were reported, respectively, by detecting the right and left interference dip closest to CWL, i.e., $D_{L,1}$ and $D_{H,1}$. Thus, a maximum sensitivity of 128,055.7 nm/RIU was achieved by measuring the wavelength separation variations between these two interference dips. This CWL-based two-mode microfiber was further applied in an immunoglobulin G (IgG) level measurement. The limits of detection of 10 fg/mL of IgG in phosphate-buffered saline solution were achieved in the experiments. Luo et al. [36] reported a refractive index sensor fabricated by tapering a single stress-applying fiber (SSAF), where a stress-applying part was introduced into the fiber cladding to engineer the cladding material index. The SSAF-based two-mode microfiber could significantly reduce the sensitivity of the group effective refractive index difference between the two interference modes— HE_{11} and TE_{01} . Therefore, the operation bandwidth of the two-mode microfiber can be broadened to 500 nm, compared with that of conventional

SMF-based two-mode microfiber with the same diameter operating at CWL. By detecting the wavelength separation changes between $D_{L,1}$ and $D_{H,1}$, a maximum sensitivity of 30,563 nm/RIU was reported in the refractive index measurement range of 1.3212~1.3216.

The interference fringes in the transmission spectrum of a CWL-existed few-mode microfiber structure can also be applied in vibration measurement. Luo et al. [35] demonstrated a highly sensitive vibration sensor using a CWL-existed two-mode microfiber MZI and packaging it in a rectangular through-hole cantilever beam. By detecting the interference dip near the CWL, the maximum axial-strain sensitivity reached $-45.55 \text{ pm}/\mu\epsilon$. This structure was also applied in acceleration sensing experiments, where the acceleration sensitivity of the sensor was 0.764 V/g at 45 Hz.

The sensors employing the CWL-based in-line MZI structures and measuring the wavelength shifts in the interference peaks/dips closest to the CWL on both sides are listed in Table 1. Compared with SFS structures, the few-mode microfibers exhibit higher sensitivity in temperature, axial strain, acceleration, and surrounding refractive index measurements. However, the taper structures and ultrasmall waists of the microfibers may cause structural fragility. Therefore, the microfibers and the taper regions should be packaged carefully to guarantee robustness in applications. During experiments, the noise induced by temperature fluctuations and axial strain in the packaging process should also be considered. The CWL-based in-line MZIs have advantages in that the CWL and interference fringes near the CWL exhibit different wavelength sensitivities under the same measurement and variation. Thus, the temperature- and strain-induced noises can be compensated by simultaneously detecting two or three peaks/dips.

Table 1. Performance comparisons of different CWL-existed in-line MZI sensors.

Structure	Sensor Application	Maximum Sensitivity	Refs.
Few-mode fiber	Curvature	$-0.745 \text{ nm}/\text{m}^{-1}$	[6]
Few-mode fiber	Axial Strain	43 pm/ $\mu\epsilon$	[10]
Few-mode fiber	Temperature	704 pm/ $^{\circ}\text{C}$	[10]
Cascaded few-mode fiber	temperature	1.753 nm/ $^{\circ}\text{C}$	[11]
Cascaded few-mode fiber	Static pressure	4.072 nm/MPa	[11]
Few – mode microfiber with a diameter of 2 μm	Refractive index around 1	$-69,984.3 \text{ nm}/\text{RIU}$	[28]
Few – mode microfiber with a diameter of 1.87 μm	Refractive index around 1	95,836 nm/RIU	[29]
Few – mode microfiber with a diameter of 3.57 μm	Sodium nitrate in seawater	5.98 pm/ppm	[33]
Z-shaped few-mode microfiber	Refractive index around 1.333	$1.46 \times 105 \text{ nm}/\text{RIU}$	[34]
Few-mode microfiber coated with PDMS	Temperature	38 nm/ $^{\circ}\text{C}$	[30]
Few-mode microfiber tapered by a ring-core two-mode fiber	Refractive index around 1.333	128,055.7 nm/RIU	[31]
Few-mode microfiber tapered by a single stress-applying fiber	Refractive index around 1.3212	30,563 nm/RIU	[36]
Few – mode microfiber with a diameter of 2.2 μm	Axial strain	$-45.55 \text{ pm}/\mu\epsilon$	[35]
Few – mode microfiber with a diameter of 2.2 μm	Acceleration	764 mV/g	[35]

4. Characteristics of the Achromatic Fringe in CWL-Existed in-Line MZIs and Their Applications

In the transmission spectrum of a CWL-existed in-line MZI, achromatic fringes are different from the periodically changing interference fringes and, therefore, are easy to identify. Because the achromatic fringe shifts monotonously with sensing parameters, CWL detection sensors can be applied in large-range measurements. This section reviews a demodulation method of the CWL and sensing applications employing CWL detection.

4.1. Detection Scheme of CWL in the SFS Sensing Structure

The demodulation method of the CWL in the transmission spectrum and its advantages, compared with the traditional interference peak detection, is explained in Ref. [8], using an etched SFS structure in SRI detection. Figure 10 shows the simulated transmission

spectra, the shift in CWL, and the wavelength shift in peak/dip located closest to the CWL on each side under different SRIs. The peaks/dips in both sides of CWL will move toward the CWL with increasing SRI. If SRI is measured by monitoring the wavelength shift in peaks/dips lying around the CWL, the peaks/dips will end at CWL with only a small measurement range of SRI, as shown in Figure 10. Therefore, traditional interference peak/dip wavelength detection methods limit the measurement range significantly.

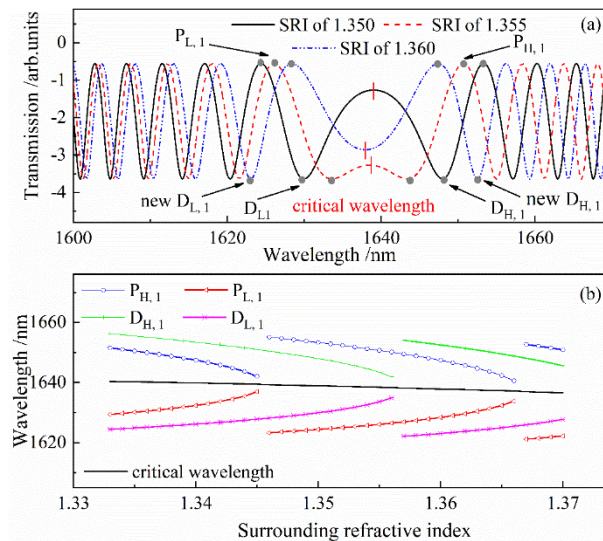


Figure 10. The simulated results of the etched SFS structure ($d_{FMF} = 21.3 \mu\text{m}$, $L_{FMF} = 20 \text{ cm}$): (a) the transmission spectra under the SRIs of 1.350, 1.355, and 1.360; (b) wavelength shifts in the critical wavelength and interference peaks/dips on each side of the critical wavelength.

Since the peaks and dips in the transmission spectrum are nearly symmetrically distributed on both sides of CWL, to avoid difficulties in identifying CWL from achromatic fringes, we can obtain CWL from Equation (8) by averaging the wavelength of $P_{H,1}$, $D_{H,1}$, $P_{L,1}$, and $D_{L,1}$, written as

$$\lambda_{CWL} = \frac{\lambda_{P_{H,1}} + \lambda_{D_{H,1}} + \lambda_{P_{L,1}} + \lambda_{D_{L,1}}}{4} \tag{8}$$

The shift in CWL with SRI is calculated from Equation (8) above, and the results are given in Figure 10b. Compared with the change in first peak or dip wavelengths simultaneously plotted in Figure 10b, the CWL changes monotonically with SRI in a large measurement range, with unambiguous demodulation of SRIs. Thus, the CWL detection sensors can effectively solve the overlapping spectrum problem and provide large sensing ranges in applications.

4.2. Sensing Applications of in-Line MZIs Based on CWL Detection

The advantages of the CWL detection method in large-range measurement are first experimentally observed in temperature detection. Tripathi et al. [18] spliced a section of MMF between two sections of SMF (SMS) and observed a CWL in the transmission spectrum at 1318 nm. The experiments showed that the CWL shifted monotonously with temperature from 25 °C to 1100 °C. Martincek et al. [40] employed a liquid-core optical fiber, which consisted of a fused silica cladding and a core with medicinal oil, to increase the temperature sensitivity of the CWL. The maximum temperature sensitivity of the measured CWL was $-56 \text{ nm}/^\circ\text{C}$, around 24 °C. The transmission spectra of the liquid-core fiber with temperature variations are shown in Figure 11.

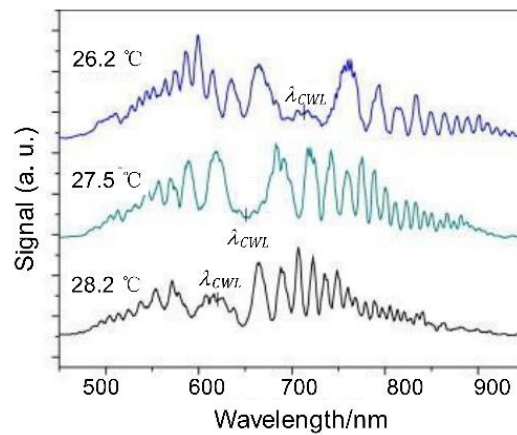


Figure 11. Shift in the CWL in MZI employing the liquid-core fiber shown on measured spectra for temperatures of 28.2, 27.5, and 26.2 °C. Reprinted with permission from Ref. [40]. Copyright 2011 Elsevier.

Our group theoretically studied the characteristics of the CWL in the transmission spectrum of an SFS structure and applied the SFS structure in the large-range measurement of SRI [8], curvature [6], and displacement measurements [7]; the sensing ranges achieved 1.316~1.44 at 1550 nm, 0~125 m⁻¹, and 0~350 mm, respectively, as shown in Figure 12.

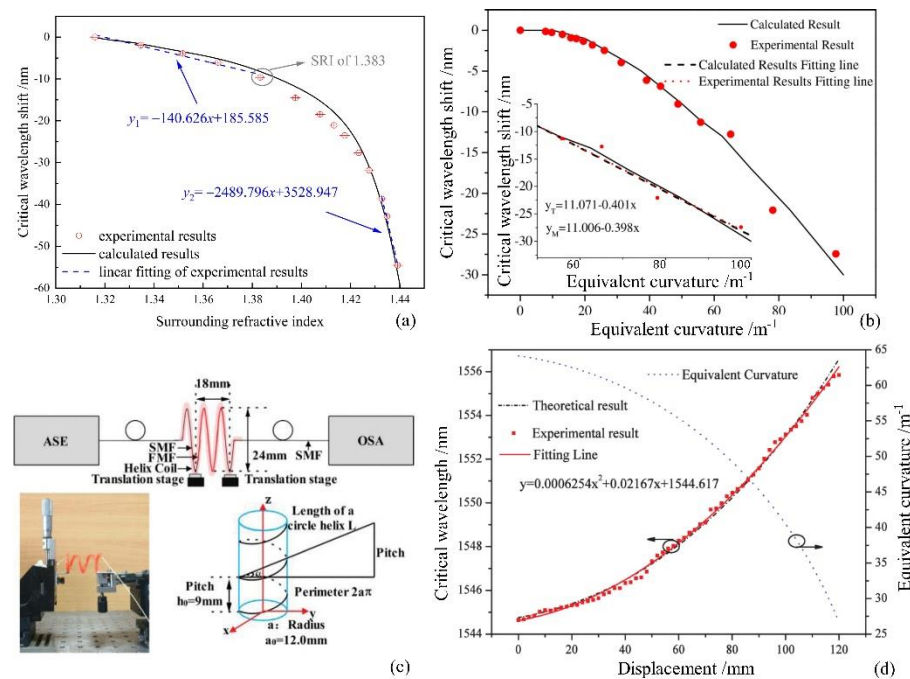


Figure 12. The wavelength shifts in CWL and sensor structures employing the few-mode fiber in the SFS structure; (a) experimental (marks with error bars) and calculated results of CWL shift with SRI variations. Reprinted with permission from ref. [8]. Copyright 2017 IEEE. (b) calculated and experimental results of CWL shift with equivalent curvature. Reprinted with permission from ref. [6]. Copyright 2016 IEEE.; (c) schematic diagram of the experiment setup of the displacement sensor employing SFS structure; (d) the experimental and the theoretical results of the CWL changes in the sensor and the theoretical equivalent curvature of FMF in the helix coil (dashed line) versus displacement. Reprinted with permission from ref. [7]. Copyright 2016 IEEE.

5. Conclusions

In this paper, we reviewed the transmission characteristics of CWL-existed in-line MZIs. The detection of the CWL in the transmission spectrum provides a solution to the overlapping problem in conventional MZIs with periodically changing interference fringes. Moreover, the interference peaks/dips on each side of the CWL shift in opposite directions. Their wavelength sensitivities increase significantly when peak wavelengths approach the CWL, which provides a solution for fiber-optic MZIs to enhance their sensitivities by designing the operational wavelength near the CWL. Therefore, taking full advantage of the CWL-existed transmission spectrum, these in-line MZIs can be developed into several different sensors, including large-range measurement sensors, multiparameter sensors, and high-sensitivity sensors, to satisfy the requirements in practical applications.

Author Contributions: Principal writing—C.L.; modification and editing—X.D., C.W. and C.L.; project administration, X.D. and C.W.; funding acquisition, X.D. and C.W. All authors have read and agreed to the published version of the manuscript.

Funding: This research was funded, in part, by the PI Project of Southern Marine Science and Engineering Guangdong Laboratory (Guangzhou) under grant number GML2021GD0808; in part, by the National Natural Science Foundation of China, grant number 61775186; and in part by the Marine and Fisheries Bureau of Xiamen, grant number 16CZB025SF03.

Institutional Review Board Statement: Not applicable.

Informed Consent Statement: Not applicable.

Conflicts of Interest: The authors declare no conflict of interest.

References

1. Li, X.; Chen, N.; Zhou, X.; Gong, P.; Wang, S.; Zhang, Y.; Zhao, Y. A review of specialty fiber biosensors based on interferometer configuration. *J. Biophotonics* **2021**, *14*, e202100068. [[CrossRef](#)] [[PubMed](#)]
2. Bhardwaj, V.; Kishor, K.; Sharma, A.C. Tapered optical fiber geometries and sensing applications based on Mach-Zehnder interferometer: A review. *Opt. Fiber Technol.* **2020**, *58*, 102302. [[CrossRef](#)]
3. Zhao, Y.; Zhao, H.; Lv, R.-Q.; Zhao, J. Review of optical fiber Mach-Zehnder interferometers with micro-cavity fabricated by femtosecond laser and sensing applications. *Opt. Lasers Eng.* **2019**, *117*, 7–20. [[CrossRef](#)]
4. Min, R.; Liu, Z.; Pereira, L.; Yang, C.; Sui, Q.; Marques, C. Optical fiber sensing for marine environment and marine structural health monitoring: A review. *Opt. Laser Technol.* **2021**, *140*, 107082. [[CrossRef](#)]
5. Wang, L.; Yj, W.; Song, S.; Li, F. Overview of fibre optic sensing technology in the field of physical ocean observation. *Front. Phys.* **2021**, *9*, 745487. [[CrossRef](#)]
6. Su, J.; Dong, X.; Lu, C. Characteristics of few mode fiber under bending. *IEEE J. Sel. Top. Quantum Electron.* **2016**, *22*, 139–145. [[CrossRef](#)]
7. Su, J.; Dong, X.; Lu, C. Property of bent few-mode fiber and its application in displacement sensor. *IEEE Photonics Technol. Lett.* **2016**, *28*, 1387–1390. [[CrossRef](#)]
8. Lu, C.; Dong, X.; Su, J. Detection of refractive index change from the critical wavelength of an etched few mode fiber. *J. Lightwave Technol.* **2017**, *35*, 2593–2597. [[CrossRef](#)]
9. Lu, C.; Su, J.; Dong, X.; Sun, T.; Grattan, K.T.V. Simultaneous measurement of strain and temperature with a few-mode fiber-based sensor. *J. Lightwave Technol.* **2018**, *36*, 2796–2802. [[CrossRef](#)]
10. Lu, C.; Su, J.; Dong, X.; Lu, L.; Sun, T.; Grattan, K.T.V. Studies on temperature and strain sensitivities of a few-mode critical wavelength fiber optic sensor. *IEEE Sens. J.* **2019**, *19*, 1794–1801. [[CrossRef](#)]
11. Lu, C.; Dong, X.; Lu, L.; Guan, Y.; Ding, S. Label free all-fiber static pressure sensor based on Vernier effect with temperature compensation. *IEEE Sens. J.* **2020**, *20*, 4726–4731. [[CrossRef](#)]
12. Su, J.; Dong, X.; Lu, C. Intensity detection scheme of sensors based on the modal interference effect of few mode fiber. *Measurement* **2016**, *79*, 182–187. [[CrossRef](#)]
13. Lei, X.; Dong, X.; Lu, C. Sensitive humidity sensor based on a special dual-mode fiber. *IEEE Sens. J.* **2019**, *19*, 2587–2591. [[CrossRef](#)]
14. Lei, X.; Dong, X.; Lu, C.; Sun, T.; Grattan, K.T.V. Underwater pressure and temperature sensor based on a special dual-mode optical fiber. *IEEE Access* **2020**, *8*, 146463–146471. [[CrossRef](#)]
15. Salik, E.; Medrano, M.; Cohoon, G.; Miller, J.; Boyter, C.; Koh, J. SMS fiber sensor utilizing a few-mode fiber exhibits critical wavelength behavior. *IEEE Photonics Technol. Lett.* **2012**, *24*, 593–595. [[CrossRef](#)]
16. Wu, Q.; Semenova, Y.; Wang, P.; Farrell, G. High sensitivity SMS fiber structure based refractometer—Analysis and experiment. *Opt. Express* **2011**, *19*, 7937–7944. [[CrossRef](#)]

17. Zhou, J.; He, B.; Gu, X. Transmission spectrum characteristics for a single-mode-multimode-single-mode fiber filter. *IEEE Photonics Technol. Lett.* **2014**, *26*, 2185–2188. [[CrossRef](#)]
18. Tripathi, S.M.; Kumar, A.; Marin, E.; Meunier, J. Critical Wavelength in the Transmission Spectrum of SMS Fiber Structure Employing GeO₂-Doped Multimode Fiber. *IEEE Photonics Technol. Lett.* **2010**, *22*, 799–801. [[CrossRef](#)]
19. Kumar, M.; Kumar, A.; Tripathi, S.M. A comparison of temperature sensing characteristics of SMS structures using step and graded index multimode fibers. *Opt. Commun.* **2014**, *312*, 222–226. [[CrossRef](#)]
20. Tripathi, S.M.; Kumar, A.; Varshney, R.K.; Kumar, Y.B.P.; Marin, E.; Meunier, J.P. Strain and temperature sensing characteristics of single-mode–multimode–single-mode structures. *J. Lightwave Technol.* **2009**, *27*, 2348–2356. [[CrossRef](#)]
21. Gonthier, F.; Lacroix, S.; Ladouceur, F.; Black, R.J.; Bures, J. Circularly symmetric modal interferometers: Equalization wavelength and equivalent step determination for matched-cladding fibers. *Fiber Integr. Opt.* **1989**, *8*, 217–225. [[CrossRef](#)]
22. Zhou, A.; Li, G.; Zhang, Y.; Wang, Y.; Guan, C.; Yang, J.; Yuan, L. Asymmetrical twin-core fiber based michelson interferometer for refractive index sensing. *J. Lightwave Technol.* **2011**, *29*, 2985–2991. [[CrossRef](#)]
23. Gu, B.; Yin, M.-J.; Zhang, A.P.; Qian, J.-W.; He, S. Low-cost high-performance fiber-optic pH sensor based on thin-core fiber modal interferometer. *Opt. Express* **2009**, *17*, 22296–22302. [[CrossRef](#)] [[PubMed](#)]
24. Yi, D.; Huo, Z.; Geng, Y.; Li, X.; Hong, X. PDMS-coated no-core fiber interferometer with enhanced sensitivity for temperature monitoring applications. *Opt. Fiber Technol.* **2020**, *57*, 102185. [[CrossRef](#)]
25. Wong, W.C.; Chan, C.C.; Chen, L.H.; Li, T.; Lee, K.X.; Leong, K.C. Polyvinyl alcohol coated photonic crystal optical fiber sensor for humidity measurement. *Sens. Actuators B Chem.* **2012**, *174*, 563–569. [[CrossRef](#)]
26. Lacroix, S.; Gonthier, F.; Black, R.J.; Bures, J. Tapered-fiber interferometric wavelength response: The achromatic fringe. *Opt. Lett.* **1988**, *13*, 395–397. [[CrossRef](#)]
27. Luo, H.; Sun, Q.; Li, X.; Yan, Z.; Li, Y.; Liu, D.; Zhang, L. Refractive index sensitivity characteristics near the dispersion turning point of the multimode microfiber-based Mach–Zehnder interferometer. *Opt. Lett.* **2015**, *40*, 5042–5045. [[CrossRef](#)]
28. Zhang, N.M.Y.; Li, K.; Zhang, N.; Zheng, Y.; Zhang, T.; Qi, M.; Shum, P.; Wei, L. Highly sensitive gas refractometers based on optical microfiber modal interferometers operating at dispersion turning point. *Opt. Express* **2018**, *26*, 29148–29158. [[CrossRef](#)]
29. Sun, L.P.; Huang, T.; Yuan, Z.; Lin, W.; Xiao, P.; Yang, M.; Ma, J.; Ran, Y.; Jin, L.; Li, J.; et al. Ultra-high sensitivity of dual dispersion turning point taper-based Mach-Zehnder interferometer. *Opt. Express* **2019**, *27*, 23103–23111. [[CrossRef](#)]
30. Xia, F.; Zhao, Y.; Zheng, H.K.; Li, L.K.; Tong, R.J. Ultra-sensitive seawater temperature sensor using an FBG-cascaded microfiber MZI operating at dispersion turning point. *Opt. Laser Technol.* **2020**, *132*, 106458. [[CrossRef](#)]
31. Sun, B.; Wang, Y. High-sensitivity detection of IgG operating near the dispersion turning point in tapered two-mode fibers. *Micromachines* **2020**, *11*, 270. [[CrossRef](#)] [[PubMed](#)]
32. Xia, F.; Zhao, Y.; Peng, Y. In-line microfiber MZI operating at two sides of the dispersion turning point for ultrasensitive RI and temperature measurement. *Sens. Actuators A Phys.* **2020**, *301*, 111754. [[CrossRef](#)]
33. Yang, L.; Wang, J.; Wang, S.; Liao, Y.; Li, Y. A new method to improve the sensitivity of nitrate concentration measurement in seawater based on dispersion turning point. *Optik* **2020**, *205*, 164202. [[CrossRef](#)]
34. Zhou, W.; Wei, Y.; Wang, Y.; Li, K.; Yu, H.; Wu, Y. Ultrasensitive interferometers based on zigzag-shaped tapered optical microfibers operating at the dispersion turning point. *Opt. Express* **2021**, *29*, 36926–36935. [[CrossRef](#)] [[PubMed](#)]
35. Liu, K.; Fan, J.; Luo, B.; Zou, X.; Wu, D.; Zou, X.; Shi, S.; Guo, Y.; Zhao, M. Highly sensitive vibration sensor based on the dispersion turning point microfiber Mach-Zehnder interferometer. *Opt. Express* **2021**, *29*, 32983–32995. [[CrossRef](#)] [[PubMed](#)]
36. Xu, S.; Chang, W.; Luo, Y.; Ni, W.; Zheng, Y.; Wei, L.; Xu, Z.; Lian, Z.; Zhang, Y.a.; Huang, Y.; et al. Ultrasensitive broadband refractometer based on single stress-applying fiber at dispersion turning point. *J. Lightwave Technol.* **2021**, *39*, 2528–2535. [[CrossRef](#)]
37. Mascotte, E.H.; Hernandez, J.M.S.; Chavez, R.I.M.; Vazquez, D.J.; Guzman, A.C.; Ayala, J.M.E.; Chavez, A.D.G.; Laguna, R.R. A core-offset Mach Zehnder interferometer based on a non-zero dispersion-shifted fiber and its torsion sensing application. *Sensors* **2016**, *16*, 856. [[CrossRef](#)]
38. Ahsani, V.; Ahmed, F.; Jun, M.B.G.; Bradley, C. Tapered fiber-optic Mach-Zehnder interferometer for ultra-high sensitivity measurement of refractive index. *Sensors* **2019**, *19*, 1652. [[CrossRef](#)]
39. Gong, H.; Chan, C.C.; Zhang, Y.; Wong, W.; Dong, X. Temperature sensor based on modal interference in hollow-core photonic bandgap fiber with collapse splicing. *IEEE Sens. J.* **2012**, *12*, 1421–1424. [[CrossRef](#)]
40. Martincek, I.; Pudis, D.; Kacik, D.; Schuster, K. Investigation of intermodal interference of LP₀₁ and LP₁₁ modes in the liquid-core optical fiber for temperature measurements. *Optik* **2011**, *122*, 707–710. [[CrossRef](#)]
41. Hlubina, P.; Kadulova, M.; Ciprian, D.; Mergo, P. Temperature sensing using the spectral interference of polarization modes in a highly birefringent fiber. *Opt. Lasers Eng.* **2015**, *70*, 51–56. [[CrossRef](#)]
42. Hlubina, P.; Olszewski, J.; Martynkien, T.; Mergo, P.; Makara, M.; Poturaj, K.; Urbanczyk, W. Spectral-domain measurement of strain sensitivity of a two-mode birefringent side-hole fiber. *Sensors* **2012**, *12*, 12070–12081. [[CrossRef](#)]
43. Wei, C.; Lin, G.; Dong, X.; Tao, S. A tunable polarization-independent comb filter based on high-order mode fiber. *J. Opt.* **2013**, *15*, 055403. [[CrossRef](#)]
44. Vengsarkar, A.M.; Walker, K.L. Article Comprising a Dispersion-Compensating Optical Waveguide. U.S. Patent 5,448,674, 5 September 1995.

45. Kumar, A.; Goel, N.K.; Varshney, R.K. Studies on a few-mode fiber-optic strain sensor based on LP01-LP02 mode interference. *J. Lightwave Technol.* **2001**, *19*, 358. [[CrossRef](#)]
46. Hocker, G. Fiber-optic sensing of pressure and temperature. *Appl. Opt.* **1979**, *18*, 1445–1448. [[CrossRef](#)]
47. Shu, X.; Zhang, L.; Bennion, I. Sensitivity characteristics near the dispersion turning points of long-period fiber gratings in B/Ge codoped fiber. *Opt. Lett.* **2001**, *26*, 1755–1757. [[CrossRef](#)]
48. Tan, Y.; Sun, L.P.; Jin, L.; Li, J.; Guan, B.O. Microfiber Mach-Zehnder interferometer based on long period grating for sensing applications. *Opt. Express* **2013**, *21*, 154–164. [[CrossRef](#)]